university of groningen

faculty of science and engineering

Nonlinear Hall Measurements and Characterization on Few-Layer $ZrTe_3$

Bachelor's thesis

June 2021

Student: Thomas Dam (s3764532)

Primary supervisor: Prof. M. H. D. Guimarães, PhD

Secondary supervisor: Prof. Jagoda Sławińska, PhD

Daily supervisor: A. C. Marx, MSc

Abstract

A new group of two-dimensional (2D) van der Waals materials has recently been uncovered: the transition metal trichalcogenides (TMTs). These have hardly been studied and are promising in the application in photonic and electronic devices, such as field effect transistors. Their comparatively high stability with respect to mono-atomic 2D materials as graphene, silicene and phosphorene makes them interesting candidates for 2D devices. Also, they have a higher chemical reactivity of TMTs compared to transition metal dichalcogenides (TMDs), which inproves device funtionalization. This, and the opportunity of studying more fundamental concepts such as charge density waves (CDW) in these materials makes them attractive objects of study. In this thesis, few-layer ($\sim$100 nm thick) zirconium tritelluride ($ZrTe_3$) is characterized. $ZrTe_3$ is a very scarcely studied TMT, with a CDW below $\sim$63 K. The CDW can induce a Berry curvature dipole which can give rise to a second order Hall effect. The CDW was not observed in our measurements, which can be most attributed to the high sensitivity to impurities literature describes for CDW formation in $ZrTe_3$. However, a characterization with a resistivity-temperature graph was achieved. At low temperature a clear anisotropic resistivity was seen in the material, as expected from literature.

Contents

1 Introduction

Graphene has sparked enormous research interest in two-dimensional (2D) layered materials because of its high potential in photonic and electronic device applications [1]. However, graphene lacks a band gap, which makes application in devices such as field effect transistors difficult. Other 2D layered materials with a band gap have since been developed, like group IV element (carbon group) monolayers (silicene [2], germanene [3] and stanene [4]), group V element (nitrogen group) monolayers (phosphorene [5]) and transition metal dichalcogenides (TMDs) [6]. TMDs are 2D van der Waals materials made up of MX_2 sheets with M a transition metal atom – such as tungsten (W), molybdenum (Mo) or zirconium (Zr) – and X a chalcogenide (oxygen group) atom: sulfur (S), selenium (Se) or tellurium (Te). The advantage of the transition metal dichalcogenides over mono-atomic 2D materials is that they are more stable and more easily manufacturable [7, p. 212]. In 2015, a new group of 2D van der Waals materials was uncovered: the transition metal trichalcogenides (TMTs), with chemical formula MX_3. Dai and collaborators state that this new class of materials is hardly studied, little literature is available on these materials, and yet the material class does have interesting properties [7, p. 212]. Zirconium tritelluride ($ZrTe_3$), the focus of this thesis, is such a TMT that has rarely been studied.

As Dai et al. noted in 2016, in a more fundamental science context, TMTs also offer good testing grounds for studying charge density waves [7, p. 219]. Charge density waves are a symmetry breaking low-temperature phase of matter, somewhat similar to superconductivity. This topic will be elaborated on in *Theoretical Framework*. Symmetry breaking phases, such as CDWs, can induce a nonlinear Hall effect via a Berry curvature dipole. In the nonlinear Hall effect voltage is proportional a higher order of the current, instead of a linear current dependence. Berry curvature is another fundamental concept, introduced by Michael Berry in his 1984 paper [8]. In a simplified manner, it can be explained as a vector quantity similar to the electromagnetic vector potential but in **k**-space instead of real space. The Berry curvature dipole in a material can be measured by the nonlinear Hall effect [9].

To gain a better understanding of the role the Hall effect plays in this research, the ordinary Hall effect is introduced here. In 1879, Edwin Hall discovered that an electric current flowing through a magnetic field perpendicular to the current's flow, experiences a force. This force points both perpendicular to the flow direction of the current and perpendicular to the direction of the magnetic field lines, as seen in Figure 1. Previously to this discovery, Maxwell thought the conducting material carrying the current experienced this force, not the current itself – as written in his Electricity and Magnetism Vol. II [10], which sparked Hall's interest and superstition. Hall devised an experiment to refute Maxwell's statement and test his own hypothesis: it is the electric current itself that experiences this force, not the conductor. Hall did detect a potential difference across the width of the conducting material, proving his hypothesis. He noticed the linear relationship between this voltage and magnetic field and even suggested the flow direction of electric current from the negative to the positive pole [11].

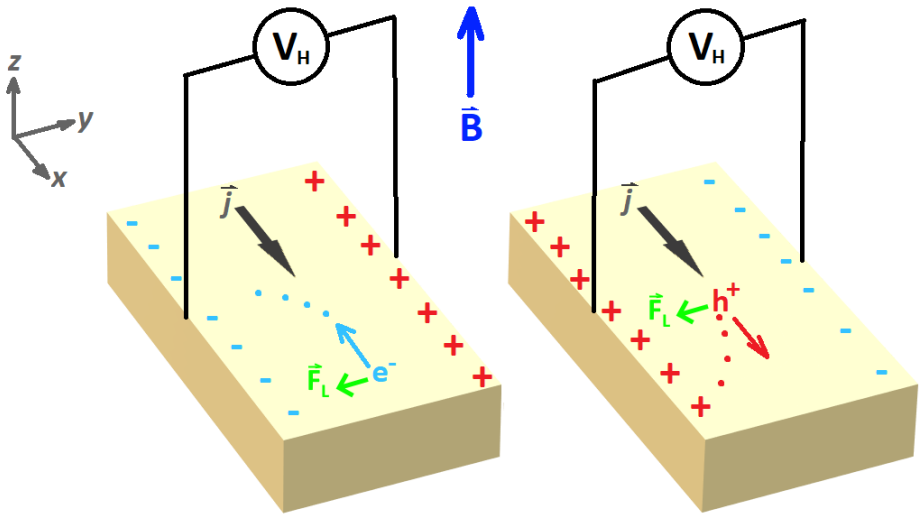

Figure 1: Two current carrying slabs with **j** in x-direction, and perpendicular homogeneous magnetic field **B** in z-direction. Electrons are shown in the left subfigure, holes in the right subfigure. Their trajectories are dotted. Note that $\mathbf{F}_L$ points in the negative y-direction for both electrons and holes.

The force Hall measured can be understood as a result of the Lorentz force $\mathbf{F}_L$ acting on the charge carriers that make up the current in the conducting material. As the Lorentz force 'bends' the trajectories of the carriers, a buildup of charge emerges on one side of the conductor while a shortage of charge emerges on the other side, giving rise to a potential difference across the conductor. This potential difference is named the Hall voltage, after its discoverer and labeled as V_H in Figure 1. Note that for differently charged carriers, the sign of the Hall voltage flips, thus making the Hall effect a useful tool for determining whether a material has a majority of positive charge carriers (holes) or negative ones (electrons).

Charge carriers experience a Lorentz force $\mathbf{F}_L = q(\mathbf{E}+\mathbf{v}\times\mathbf{B})$ because of the current generating electric field $\mathbf{E}$ and the externally applied magnetic field $\mathbf{B}$, where q is the charge of the carrier particle and $\mathbf{v}$ is its velocity. As the carriers scatter through the conductor, they lose their momentum $\mathbf{p}$ to lattice vibrations and thermal excitations (simply heat on the macroscopic scale) during a mean free time (or relaxation time) τ, modelled as a damping force $\mathbf{F}_{damping}$. As the Lorentz force and the damping force become equal and opposite, the carrier flow in the material reaches equilibrium. Thus, there will no longer be a net force and the system will remain in a steady state. The steady state equation becomes:

$$\mathbf{F}_{net} = \mathbf{F}_L + \mathbf{F}_{damping} = q(\mathbf{E} + \mathbf{v} \times \mathbf{B}) - \frac{\mathbf{p}}{\tau} = 0 \tag{1}$$

To write the electric field as a function of current density and resistivity, one can use the definition of current density $\mathbf{j} = nq\mathbf{v}$ (where n is carrier density) with $\mathbf{p} = m\mathbf{v}$ and substitute this into Eq. (1), which gives:

$$\begin{aligned} \mathbf{E} &= \frac{\mathbf{p}}{q\tau} - \mathbf{v} \times \mathbf{B} \\ &= \frac{1}{nq}\left(\frac{m}{q\tau} + \mathbf{B}\times\right)\mathbf{j}. \end{aligned} \tag{2}$$

Then, by writing the part between brackets as second-rank tensors mapping $\mathbf{j}$ to $\mathbf{E}$ we find:

$$\mathbf{E} = \frac{1}{nq}\begin{bmatrix} \frac{m}{q\tau} & -B_z & B_y \\ B_z & \frac{m}{q\tau} & -B_x \\ -B_y & B_x & \frac{m}{q\tau} \end{bmatrix}\begin{bmatrix} j_x \\ j_y \\ j_z \end{bmatrix}. \tag{3}$$

(The derivation of Eq. (3) from Eq. (2) is given in Appendix A.) The constants and the tensor in front of $\mathbf{j}$ in Eq. (3) can be replaced by a single tensor, which greatly simplifies this equation:

$$\mathbf{E} = \overleftrightarrow{\boldsymbol{\rho}}\,\mathbf{j} \qquad \text{with} \qquad \overleftrightarrow{\boldsymbol{\rho}} = \frac{1}{nq}\begin{bmatrix} \frac{m}{q\tau} & -B_z & B_y \\ B_z & \frac{m}{q\tau} & -B_x \\ -B_y & B_x & \frac{m}{q\tau} \end{bmatrix}. \tag{4}$$

Here, $\overleftrightarrow{\boldsymbol{\rho}}$ is called the resistivity tensor, which acts on $\mathbf{j}$. The the quantity $\frac{1}{nq}$ in Eq. (4) is useful, because it relates the electric field to the strength of the magnetic field. This quantity is called the Hall coefficient R_H ($R_H = \frac{1}{nq}$). Note that the standard scalar relationship between current and electric field is written as $E = \rho\, j$. However, using steady state Eq. (1) to derive a tensor form of this relationship is particularly useful in the context of this research. Namely, when unequal off-diagonal elements are found in the resistivity tensor, the resistivity tensor is said to be anisotropic, and this can signify the presence of 'Hall-like' effects. As briefly discussed before the above introduction on the Hall effect, materials with broken symmetries can give rise to a nonlinear Hall effect. This nonlinear Hall effect is such a 'Hall-like' effect that can be present in the resistivity tensor. As will be seen in the next section, $ZrTe_3$ is such a low-symmetry material.

Both the solutions TMTs pose to the problems that graphene and other mono-atomic 2D van der Waals materials have in device fabrication, the advantage of TMTs over TMDs in terms of reactivity for device functionalization [7, p. 219] and the usage of TMTs for gaining a better understanding of fundamental concepts such as Berry curvature and charge density waves, make this new class of materials a highly interesting object of study. As $ZrTe_3$ is a very little studied TMT that exhibits both superconductivity (below about 5K) and charge density waves (below about 63K), this is a particularly good candidate for the latter research goal.

2 Theoretical Framework

This section starts by explaining higher order Hall effects, then elaborates on charge density waves and superconductivity. Finally, it illustrates the crystal structure of $ZrTe_3$, explains crystal defects and how the symmetries of the crystal can give rise to Hall-like effects via Berry curvature.

2.1 Higher Order Hall Effects

The linear, ordinary Hall effect described in the *Introduction* section only occurs in systems with broken time-reversal symmetry. Conversely, there should be no ordinary Hall effect in systems that are time-reversally symmetric. This is due to Onsager's reciprocity theorem, which states that the resistivity tensor should be symmetric ($\overleftrightarrow{\boldsymbol{\rho}} = \overleftrightarrow{\boldsymbol{\rho}}^{\,T}$) when the system's Hamiltonian is invariant under time-reversal symmetry [12]. The broken time symmetry can be induced using an external magnetic field, like in the classical Hall effect originally discovered by Hall. It can also be induced by more exotic means, such as an internal magnetization of the conductive medium, which is referred to as the anomalous Hall effect (AHE) [13].

However, more exotic, higher order Hall effects are allowed even when time-reversal symmetry is not broken, because only the linear effect is constrained by Onsager's reciprocity theorem. These Hall effects can be classified as anomalous Hall effects, as they are not classical. However, this AHE is distinct from the AHE in magnetized materials described above, as it is not due to some internal magnetization. For this reason, these higher order effects are referred to as the nonlinear anomalous Hall effect (or nonlinear AHE) [13]. Sodemann and Fu [9] demonstrated that a metal with broken inversion symmetry can give rise to a nonlinear AHE, in particular the second order. This means that a metal that is time-reversally symmetric, but has broken inversion symmetry can exhibit a second harmonic Hall voltage, perpendicular to the applied current.

Assuming the Hall resistance R_{Hall} (not to be confused with Hall coefficient R_H) is not constant but dependent on current in some higher order, we can take a Taylor expansion around R(I=0) for the Hall resistance and substitute into Ohm's law:

$$V_H = R_{Hall}(I) \cdot I = (R_0 + R_1 I + R_2 I^2 + R_3 I^3 + ...) \cdot I. \tag{5}$$

For the second order Hall effect we only keep the zeroth and first order while dropping the higher order terms. Rewriting we obtain:

$$V_H = R_0 I + R_1 I^2, \tag{6}$$

and by substitution of an alternating (AC) current $I(t) = I_0 \sin(\omega t + \phi_0)$ (with amplitude I_0, frequency ω and phase ϕ_0) this gives:

$$V_H(t) = R_0 I_0 \sin(\omega t + \phi_0) + \frac{1}{2} R_1 I_0^2 + \frac{1}{2} R_1 I_0^2 \sin(2\omega t + \phi_1) \qquad \text{with} \quad \phi_1 = 2\phi_0 - \frac{\pi}{2}. \tag{7}$$

Note how the alternating voltage gains a part $\frac{1}{2} R_1 I_0^2 \sin(2\omega t + \phi_1)$ that is also time dependent – similarly to the linear part $R_0 I_0 \sin(\omega t + \phi_0)$ – but proportional to the square of the input current and has double the input frequency. This part is referred to as the second harmonic Hall voltage, and should be experimentally detectable in crystals with the required (broken) symmetries described above. The origin of the symmetry requirements will be explained in section 2.3.

2.2 Charge Density Waves and Superconductivity

Both superconductivity (SC) and charge density waves (CDWs) are low temperature phases in solid state materials. Both occur at a transition temperature T_{SC} and T_{CDW} respectively.

In the case of SC, the resistance of a material suddenly drops to zero at the transition temperature T_{SC}. This gives rise to various interesting exotic properties, such as the Meissner effect (the expelling of magnetic flux lines to outside the material, as a $\rho = 0$ material is perfectly diamagnetic) and the possibility for a current loop to flow indefinitely through the material without dissipating thermal energy [14]. Superconductivity can be considered a result of broken charge conservation symmetry at low temperatures [15].

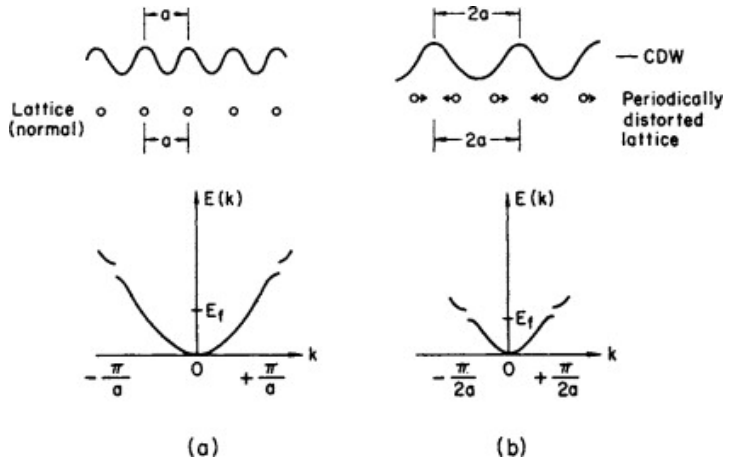

Figure 2: Formation of a CDW. Source: Adapted from [16, Fig. 34].

In 1955, Peierls pointed out that a 1D electron gas on an underlying metal lattice (shown in Fig. 2**a**, *top*) is not stable at low temperatures [17]. Correlation effects lead to phase transitions and collective modes at low temperatures, which causes this instability. To restabilize the lattice, a gap opens at the Fermi wave vectors (Fig. 2**b**, *bottom*). This in turn, causes the charge density $\rho(r)$ of the electrons around the metal ions to change (Fig. 2**b**, *top*). The lattice atoms shift position and the electrons form a standing wave pattern, called a CDW, which may be pinned on impurities in the lattice. Since 1955, research has pointed out that to some extent, Peierls model could describe well the CDW generation in 1D crystals and some quasi-2D crystals [18], [19]. In a simplified sense, $ZrTe_3$ can be treated as multiple 1D-chain system, which can explain the possibility for the formation of a CDW.

The formation of a CDW breaks the particle-hole and lattice translation symmetries in the lattice, but preserves charge conservation symmetry. On the other hand, superconductivity can be considered a result of broken charge conservation symmetry at low temperatures. Thus, both effects can be considered as two distinct symmetry breaking phases that each break other symmetries [15].

2.3 Berry Curvature

In 1984, Michael Berry published a paper on the extra phase the Hamiltonian $H(\mathbf{R})$ (depending on a parameter space $\mathbf{R}$ and time t) of a quantum system gains when it undergoes a cyclic adiabatic transformation [8]. Cyclic means the system returns to its initial state ($\mathbf{R}(\mathrm{t}) = \mathbf{R}(0)$) and adiabatic means the transition is 'smooth', similarly to a quasi-static process in thermodynamics. In the Ahronov-Bohm effect, this can be seen as a phase the electron wavefuction gains as it takes different paths around an infinitely long solenoid. Then, the magnetic field $\mathbf{B}$ along the semicircular paths is zero, but the electromagnetic vector potential $\mathbf{A}$ is non-zero along the two paths, leading to a different phase gain of the electron wavefunctions along either side of the solenoid and to an interference pattern when the two beams reunite. The extra phase is now known as the Berry phase γ, and for a system in eigenstate n with corresponding eigenvalue ϵ_n, γ_n can be expressed as an integral over a closed cyclic path C:

$$\gamma_n = \oint_{\mathcal{C}} d\mathbf{R} \cdot \mathcal{A}_n \qquad \text{where} \qquad \mathcal{A}_n = i \left\langle n(\mathbf{R}) | \nabla_R | n(\mathbf{R}) \right\rangle . \tag{8}$$

Here, $\mathcal{A}_n$ is called the Berry connection and – similarly to the electromagnetic potential – denoted by the letter A. This is not a coincidence, because just as the curl of $\mathbf{A}$ gives a useful quantity: the magnetic field $\mathbf{B}$; the curl of this $\mathcal{A}_n$ gives a mathematically useful quantity as well: the Berry curvature $\mathbf{\Omega}$. If we take the parameter space to be momentum-space or $\mathbf{k}$-space, it can be shown that for electrons in a crystal lattice:

$$\begin{aligned} \mathbf{v} &= \mathbf{v}_{drift} + \mathbf{v}_{anomalous} \\ &= \frac{1}{\hbar} \frac{\partial \epsilon_n(\mathbf{k})}{\partial \mathbf{k}} - \frac{e}{\hbar} \mathcal{E} \times \mathbf{\Omega}(\mathbf{k}) \end{aligned} \tag{9}$$

where $\mathcal{E}$ is the applied electric field, $\mathbf{v}_{drift} = \frac{1}{\hbar} \frac{\partial \epsilon_n(\mathbf{k})}{\partial \mathbf{k}}$ is the drift velocity and the part that the Berry curvature contributes to is referred to as the anomalous velocity $\mathbf{v}_{anomalous}$. As seen in Eq. (9), the presence of a nonzero Berry curvature can invoke an anomalous velocity in electron flow through a crystal. This anomalous velocity is perpendicular to the applied electric field, which causes non-zero off-diagonal elements in the resistivity tensor. Thus, the second order Hall effect from section 2.1 can be explained by the underlying phenomenon of a non-zero Berry curvature. Hence, second order Hall effect induced in a material can be a direct measure of the Berry curvature of that material (in particular on the Berry curvature dipole moment [9]).

The symmetry requirements mentioned in section 2.1 can also be explained by symmetries of the Berry curvature. Take for example, a crystal that has time-reversal symmetry as well as spatial inversion symmetry in $\mathbf{k}$-space. That would mean both the following equations must be satisfied:

$$\begin{aligned} \mathbf{\Omega}(\mathbf{k}) &= -\mathbf{\Omega}(-\mathbf{k}) \qquad \text{(time reversal symmetry)} \\ \mathbf{\Omega}(\mathbf{k}) &= \mathbf{\Omega}(-\mathbf{k}) \qquad \text{(inversion symmetry)} \end{aligned} \tag{10}$$

and thus $-\mathbf{\Omega}(-\mathbf{k}) = \mathbf{\Omega}(-\mathbf{k})$, which means the Berry curvature would have to be zero, leading to zero anomalous velocity and no Hall effect.

2.4 Properties of $ZrTe_3$

2.4.1 Crystal Structure

$ZrTe_3$ is a 2D van de Waals transition metal trichalcogenide (TMT) that crystallizes in a structure made up of long trigonal prismatic $ZrTe_3$ chains in the crystal b direction, arranged in pairs along their length direction, as shown in the outlined monoclinic unit cell in Fig. 3**a**. The pairs then form sheets in the ab-plane. In Fig. 3**a** the gray triangles outline the cross section of these chains and three of the chains are shown in Figure 3**b**. The prismatic chains are held together by Te-Te interactions orthogonal to the direction of these chains, which are modelled as a combination of a $(Zr^{4+})(Te^{2-})(Te_2^{2-})$ state and a $(Zr^{2+})(Te^{2-})(Te_2)$ state by Felser and colleagues [20, p. 1787]. Note how neighboring chains are translated with respect to each other by $b/2$ along the b direction (Fig. 3**b**) [20, p. 1788]. The sheets are held together by van der Waals interactions. The lattice parameters of this material are $a = 0.587$ nm, $b = 0.391$ nm and $c = 1.01$ nm with $\alpha = \beta = 90°$ and $\gamma = 98.00°$ [20, p. 1789].

2.4.2 Electronic Properties

$ZrTe_3$ classifies as a metal. Felser and colleagues report a resistivity of about 75 µΩ·cm in the a and about 140 µΩ·cm b direction at room temperature [20]. Other literature by Zhu et al. reports a resistivity that is aproximately equal in the a and b direction, of about 120 ± 20 µΩ·cm [21]. $ZrTe_3$ has a transition to a CDW state at around 65K and a SC state below ~5.2K (poly-crystals) or ~4K (single crystals) at ambient pressure [22], [23]. The SC and CDW may occur simultaneously at ambient pressure, but compete when the material is under high pressure (above ~5 GPa CDW is suppressed while the SC state reappears) [24]. The CDW formation is sensitive to crystallographic defects: both intercalation (placement of foreign atoms between van der Waals sheets) of Cu and Ag between the $ZrTe_3$ sheets and substitution of trace amounts of Se en lieu of Te suppress the CDW [22], [25]. The CDW can be detected by a 'bump' in the temperature-dependent resistivity graph – in this case around 63 K for bulk $ZrTe_3$ – that appears as the lattice atoms shift (see Fig. 3**c**).

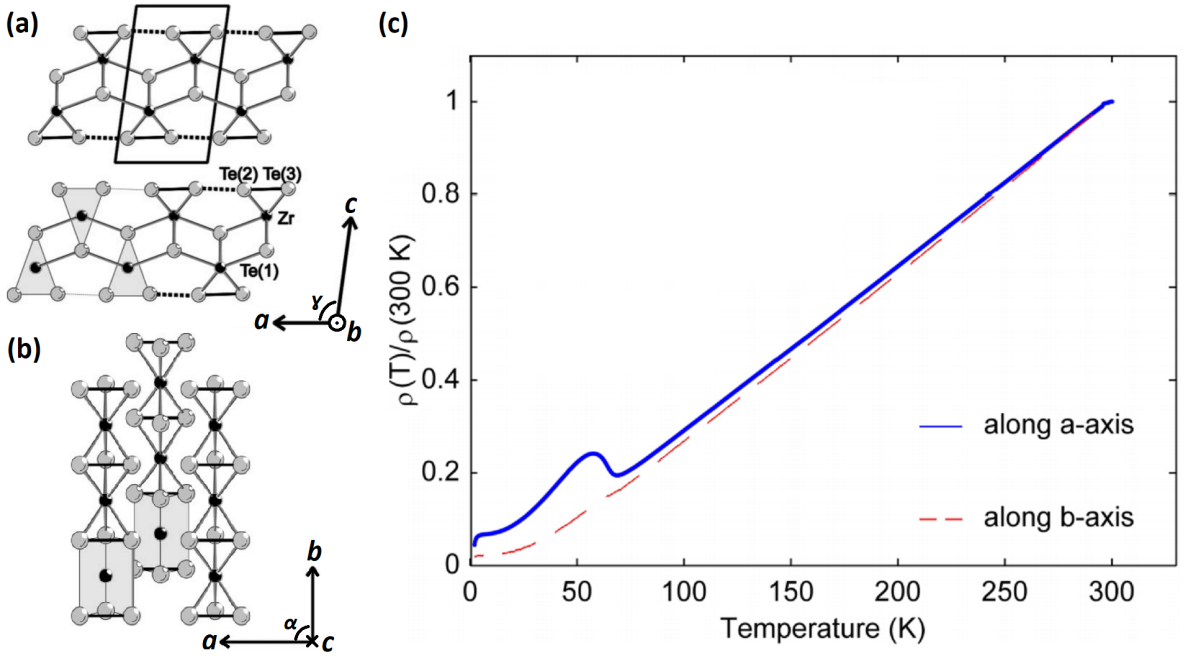

Figure 3: Crystal structure of $ZrTe_3$ in ac-plane (**a**) and ab-plane (**b**). Source: Adapted from [20, Fig. 1]. Graph of measured resistivity data to temperature of $ZrTe_3$ with charge density wave signature in the crystal a-direction around $T = 63$ K (**c**). Source: Adapted from [26, Fig. 1(b)].

2.4.3 Crystal Symmetries

As explained in section 2.2, a low symmetry material can give rise to a Berry curvature dipole, which in turn can induce a second order Hall effect. Especially materials that have a broken inversion symmetry show this behavior. Because of the high anisotrosopy of the material, $ZrTe_3$ has only one mirror plane and one glide plane: a 180 degree rotation followed by a translation of $\frac{1}{2}$ the lattice vector. As the CDW that occurs in $ZrTe_3$ distorts the lattice, this can break the mirror plane symmetry and allow a non-negative Berry curvature. Consequently, a second order Hall effect may be detected.

2.4.4 Crystal Defects and Residual Resistance Ratio

As mentioned in the previous subsection, CDW formation in $ZrTe_3$ is sensitive to crystallographic defects. Crystallographic defects are distortions in the periodicity of a crystal. These defects can be point defects, like impurities (foreign atoms Y substituted in a crystal lattice composed of atoms X) and vacancy defects (atoms missing from the crystal lattice); line defects such as dislocations and screw dislocations; or planar defects such as grain boundaries [27].

The more defects there are in a crystalline material, the more scattering events occur per electron per unit time, which slows the overall flow of electrons through the lattice and hence microscopically manifests as an increase in resistance of the material. As explained in the previous section, at $T = 0$ K, many materials are superconducting and their resistivity should be equal to zero. Thus, when a material is cooled down nearing absolute zero, all remaining resistivity measured can be attributed to crystallographic defects. When this remaining resistivity is normalised over the resistivity at room temperature, this ratio can be used as a measure of purity and general quality of a sample. This ratio is called the residual-resistance ratio (RRR) and is defined as $RRR = \frac{\rho(T=300\text{K})}{\rho(T=0\text{K})}$.

3 Research Methods

In this section the research techniques are treated. First, the fabrication of the sample is explained, including a concise description of each fabrication step and the techniques used. Then, the measurement techniques used to test the predictions mentioned in the *Theoretical Framework* section are elaborated on.

3.1 Sample Fabrication

To measure the electronic properties of $ZrTe_3$, we fabricated a microscopic Hall device (Fig. 4**d**). The device has a longitudinal pair of contacts (contacts *a* and *e* in Fig. 4**c**) and three pairs of transverse contacts (contact pairs *b* & *h*, *c* & *g*, *d* & *f* in Fig. 4**c**). The layout of the contacts is chosen such that if a pair of transverse contacts is dysfunctional, another pair can be used for measurement. Also, the different distances between transverse pairs can be used to determine the resistivity in the longitudinal direction when flake thickness is determined.

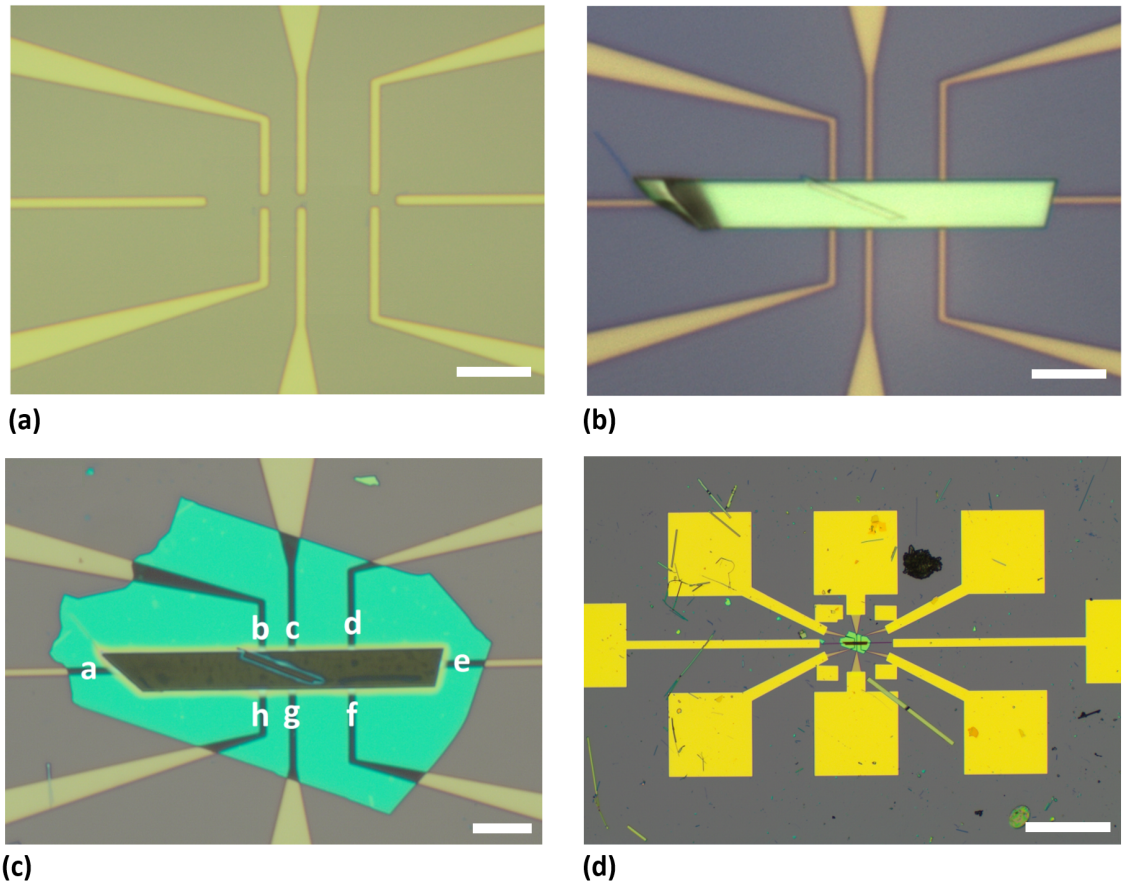

Figure 4: Optical microscope images of: the bare Pt contacts before flake transfer (**a**); the unfinished sample with $ZrTe_3$ flake (faded green) transferred onto Pt contacts (**b**); the finished sample with $ZrTe_3$ flake (gray) on top of which the hBN flake (cyan) is placed (**c**); and an overview of the entire device with gold contacts (yellow) visible (**d**). The contacts are marked from *a* to *f* (in white) (**c**). (Scale bars in **a**, **b** and **c** are 10 microns, scale bar in **d** is 200 microns.)

3.1.1 Contact Fabrication

The contacts were patterned on a Si substrate with a 285 nm SiO_2 layer using the lift-off process. The device has two layers of contacts: eight platinum (Pt) contacts in the centre of the substrate (small contacts, Fig. 4**a,b,c**) and a series of gold (Au) contacts surrounding and connected to these (large contacts, Fig. 4**d**). To create each set of contacts with this process, first a bilayer of positive photoresist is spin coated onto the substrate. After this step, the contacts are patterned into the photoresist by exposing it with an electron beam (e-beam lithography or EBL). After exposure, the exposed area of the resist is washed away using a solvent (development) and the substrate is ready for deposition. A layer of titanium (Ti) is deposited on the substrate before the Pt or Au is sputtered onto it. This is done to decrease the pressure in the sputtering chamber further [28], and to make the Pt and Au adhere better to the substrate. After Ti and Pt was deposited to the desired thickness, the photoresist is washed away (or lifted off, hence the 'lift-off' process) and only a clean sample with the small contacts remains. The entire process is then repeated with Au to add the large contacts to the substrate. The Pt contacts are 10 nm thick with a bottom 1 nm layer composed of Ti. The large contacts are made of an Au-layer of 50 nm with a Ti-layer of 5 nm underneath.

3.1.2 Exfoliation

First, a 56 microns long and 6.3 microns wide flake of $ZrTe_3$ was exfoliated (Fig. 4**a**). Exfoliation is a process in nanofabrication where a macroscopic piece of the desired material is put on top of adhesive tape, after which it is folded several times to tear the macroscopic material up into smaller, microscopic parts or flakes. The tape is then pressed on top of a cleaned silicon (Si) substrate and removed, such that a desired flake can be searched for on the substrate using an optical microscope. Note that flake colours seen through the microscope are no true colors, but indicate the thickness of the flake by refraction of the white microscope light. This means the color of the flakes seen under the microscope can be used to select a flake of roughly the desired thickness.

3.1.3 Flake Transfer

We exfoliated $ZrTe_3$ on a polydimethylsiloxane (PDMS, a type of silicone) stamp and transferred a suitable flake of $ZrTe_3$ onto the set of nanofabricated contacts (Fig. 4**a**). Using polycarbonate (PC) film on a PDMS stamp on a glass slide, a hexagonal boron nitride (hBN) flake was lifted and placed on top of the $ZrTe_3$ flake (in Fig. 4**c**). The bare contacts without flake are shown in Fig. 4**b**, with dimensions indicated. The pick-up technique used is similar to the technique for graphene-hBN heterostructures, as explained in an article by Zomer et al. [29]. The hBN is placed on top of the $ZrTe_3$ to prevent it from oxidation, which is expected to occur within several hours when exposed to air. For this same reason, all exfoliation and transferring was done in an air-sealed (oxygen and moisture free) glove box.

3.2 Measurement Techniques

3.2.1 Equivalent Circuit and Multiple Probe Measurements

The anisotropic resistances through the flake can be schematically represented by an equivalent circuit diagram. This circuit diagram is shown in Fig. 5**a**. Yellow indicated resistances are the contact resistances R_{Cx} (with x a contact), while the indigo indicated resistances R_{Fx} are the anisotropic flake resistances. To clear up an ambiguity: the contact resistance measured is not the resistance the current flowing through the contacts experiences, but the resistance the current experiences when transitioning between the contacts and the flake.

Before conducting measurements in a temperature sweep, the quality of the contacts had to be checked and it had to be checked whether the contact connections were Ohmic (their I-V curve is linear). For this, 2-probe, 3-probe and 4-probe measurement arrangements were used. A 2-probe measurement is a measurement with only two connection points: an I_+V_+ connection and an I_-V_- connection. A 4-probe measurement has four connection points: I_+, I_-, V_+ and V_-, all being separately connected to the measurement apparatus. A 3-probe measurement has three connection points, all four probes separately connected with exception to V_+ or V_- being connected to either the current source or current drain connector [30].

For currents that are only applied longitudinally in a 2-probe arrangement, we assume no transverse resistance component is felt by the current, for example a current applied from contact c to d. This changes the circuit diagram to the one in Fig. 5**b**:

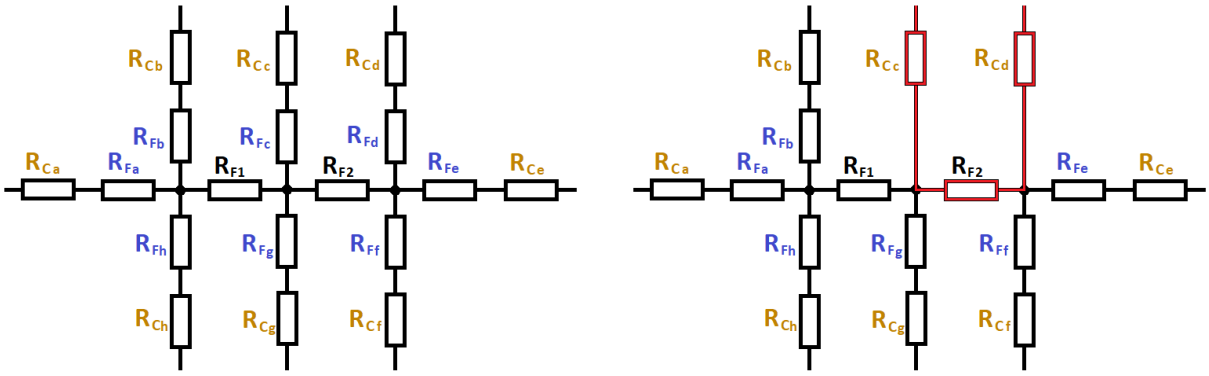

(a) (b)

Figure 5: Equivalent circuit for the $ZrTe_3$ device (**a**) and modified circuit in the case of a strictly longitudinally applied current in 2-probe configuration, in this example over contacts c and d (**b**).

3.2.2 Temperature Sweep

To do the temperature dependent resistivity measurement as described in Theory, the sample was placed in a vacuum chamber and cooled with liquid helium, as seen in Fig. 6. After the substrate was sufficiently cooled and temperature stabilized (to between 5K and 10K, varying with each measurement), it was slowly heated by a heating unit (h in Fig. 6). At each measurement point the voltage over the $ZrTe_3$ flake was measured as a function of temperature. The current was held constant. Subsequently, we determined the resistance and resistivity from the voltage and current data obtained from measurement.

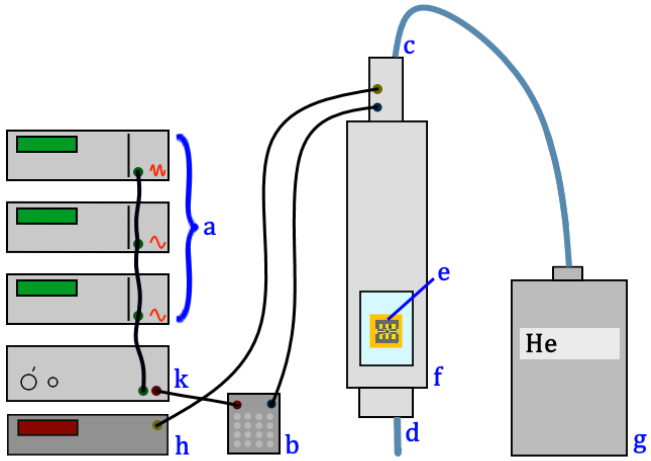

Figure 6: Experimental setup diagram with lock-in amplifiers (a) connected to the chip carrier with sample (e) via a switch box (b) via an amplifier (k). The vacuum chamber (f) is cooled with a liquid He Dewar (g) via the He inlet (c) and re-heated with a heater (h). The He outlet is labeled as d.

We did the temperature sweep measurements using a set of lock-in amplifiers connected to the sample on a chip carrier via a switch box. The current applied to the contacts was slowly increased to the selected AC current used for the measurement, to prevent a spark caused by quickly increased current. Previous to each measurement a set frequency was selected (not a multiple of 50Hz or close to this, as this is the power grid frequency). For the entire temperature sweep, the current was held constant and the voltage over the selected contacts was measured. Two lock-in amplifiers measured the voltage, one first harmonic signal and the other second harmonic signal. A third lock-in amplifier either measured the longitudinal voltage where the current was applied, measured the transverse voltage where current was applied or was not used at all.

The first harmonic or fundamental frequency is a measurement of the voltage signal with the input frequency. The second order signal is measured with a frequency double this input frequency, as a result of the nonlinear Hall effect described in section 2.1. In example, a current source of 200 µA was applied from contact *e* to *a*, the first harmonic voltage signal was measured over contacts *c* and *d*, and the second harmonic voltage signal was measured over *d* and *f*.

3.2.3 Atomic Force Microscopy

The thickness of the device (and the $ZrTe_3$ flake) is measured using atomic force microscopy (AFM). AFM works by the principle of tapping the substrate surface with a microscopic golden or platinum cantilever tip, analogous to a finger sensing a rough surface. Because of the few-atom wide tip, near-atomic resolution can be achieved. A feedback loop makes sure the distance between tip and substrate is either held constant or oscillating constantly (in tapping mode). The tip position is controlled by piezo-tubes and measured by a laser interferometer.

4 Results

This section presents the results from the experiments described in the previous section. Firstly, thickness of the flake is determined from the AFM measurements and used to estimate the resistivity of $ZrTe_3$. Then, the various probe measurement results are presented to show an Ohmic resistance, validating the further measurements. After that, the contact resistance is estimated and calculated. Finally, the temperature-dependent resistivity measurements are presented, together with the calculation of the RRR in both crystal directions.

4.1 Resistivity and Flake Thickness with AFM

Fig. 7 shows the pictures obtained from AFM. From the AFM cross sections in Fig. 7**c** it can be seen that the flake thickness of the entire $ZrTe_3$ flake is 105 ± 10 nm. The width of the flake can also be determined from the cross sections in Fig. 7**c**: w = 8.2 ± 0.5 µm. This yields a cross sectional area of A = (86.1 ± 9.7)·10^{-14} m^2. The resistance of part of the flake between contacts b and d is estimated to be R_{FT} = 17.1 ± 0.6 Ω (see Appendix B for the estimation). The distance l between contacts b and d is 15 µm (see Fig. 4 in *Research Methods*). Now, one can use the ideal case definition of resistivity $\rho = R\frac{A}{l}$ and substitute all above parameters into this equation. This this gives a longitudinal resistance of ρ_b = (9.8 ± 1.2)·10^{-7} Ω m = 98 ± 12 µΩ cm.

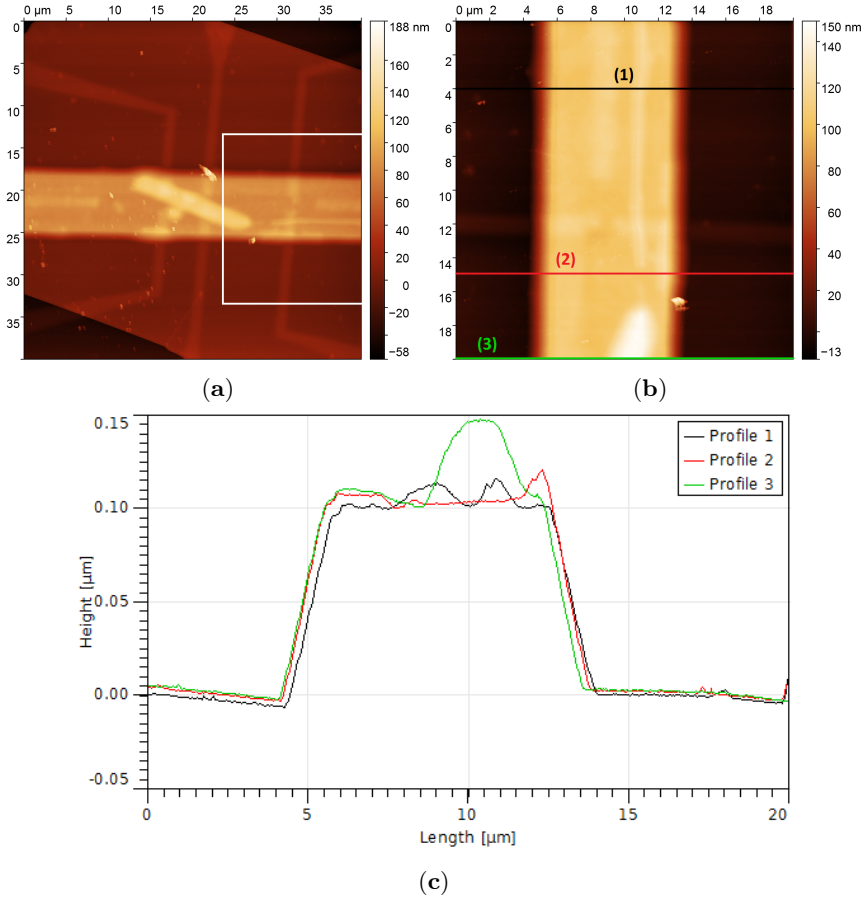

(**a**) (**b**)

(**c**)

Figure 7: AFM image of the device (**a**), zoomed in part of the flake (**b**) and three cross sections of the $ZrTe_3$ flake (**c**). The three height profiles in (**c**) are taken from the colored sections indicated in (**b**). The white square in (**a**) indicates the zoomed part in (**b**).

Height profile 3 in Fig. 7**c** shows a sudden increase in height. Indeed, the flake seems to have a small second flake of $ZrTe_3$ on top of it (colored yellow in 7**a**), somewhat aligned in between contacts b and g. Here, the flake thickness extends another 45 nm. This anomaly is assumed to not influence the resistivity significantly and thus neglected in the resistivity estimation.

4.2 Ohmic Test

To check whether the contacts were Ohmic, current-voltage sweeps were performed over each adjacent pair of contacts in a 2-probe configuration. Also, each opposing pair of contacts was tested in a 2-probe configuration. Three of these twelve current-voltage sweeps are shown below in Fig. 8. Note the linearity of the blue I-V curves, indicating the linear relationship between current and voltage and hence confirming that the flake and contact resistances are Ohmic.

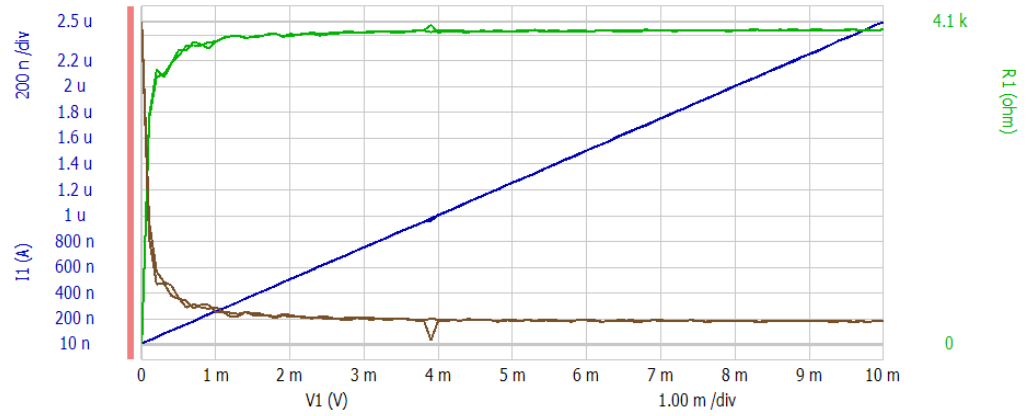

(**a**)

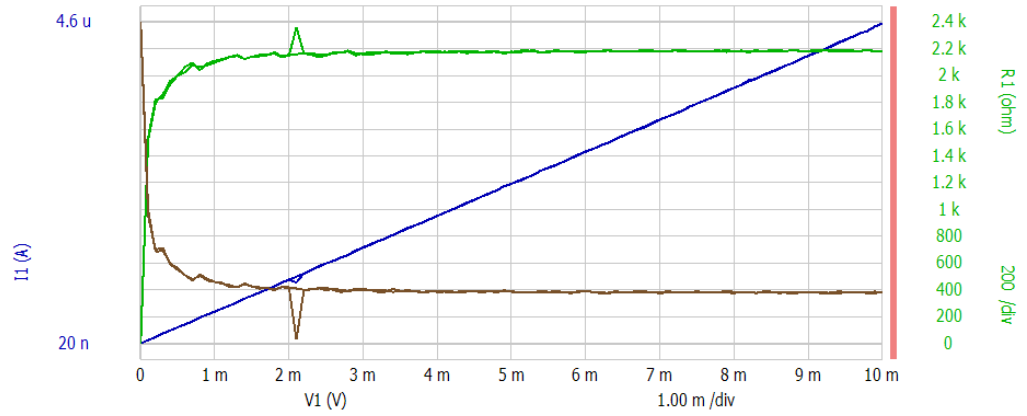

(**b**)

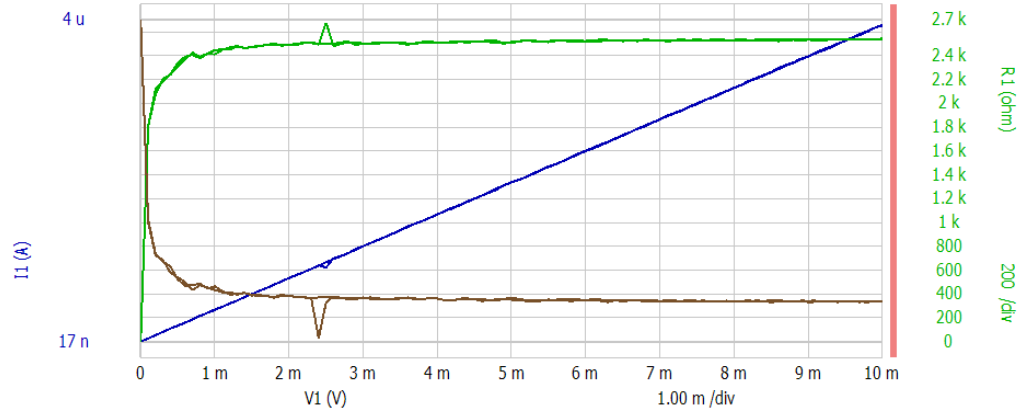

(**c**)

Figure 8: Three of the current-voltage sweeps performed, with blue I-V curve, green R-V curve and brown G-V curve. The graphs for the a-e pair (**a**), c-g pair (**b**) and f-g pair (**c**) are shown.

4.3 Contact Resistance

The contact resistance is estimated by subtracting the resistance of the flake from the total resistance along path *a*-*e*, and dividing this by two. The flake resistance is estimated to be $R_F = R_{FT} \cdot \frac{26\mu m}{15\mu m} = 29.6 \pm 1\ \Omega$ (see Appendix B). The entire resistance along path *a*-*e* is found to be 1.96 ± 0.1 kΩ. The resistance for one contact (assuming that all contacts have the same resistance) is then found to be 0.97 ± 0.1 kΩ.

4.4 Temperature Sweeps and *RRR*

The relative resistivity (ρ(T)/ρ(300K)) to temperature graphs are shown in Fig. 9 for the crystal *a*-direction (blue) and *b*-direction (red). The longest side of the flake is expected to be the crystal *b*-direction, along the length direction of the 1D $ZrTe_3$ chains. The sheets are stacked in the *c*-direction, so the second in-plane direction seen is the *a*-direction. The bottom right inset indicates the *a*- and *b*-directions on the substrate.

The data set for the *a*-direction was acquired by a 4-probe measurement. The current was applied from contacts *a* to *e* and the voltage was measured over contacts *c* and *d*. This assures that the potential difference is only measured over the $ZrTe_3$ flake and the contact resistances are excluded. For the data set in the *a*-direction, a 4-probe measurement with exclusion of contact resistance was not possible. To only measure the voltage over the flake, a 2-probe measurement was done, and the contact resistances estimated above were subtracted from the data set. For this 2-probe measurement the contact pair *d*-*f* was chosen, to make sure that the anomaly mentioned in 4.1 would influence the measurement as little as possible.

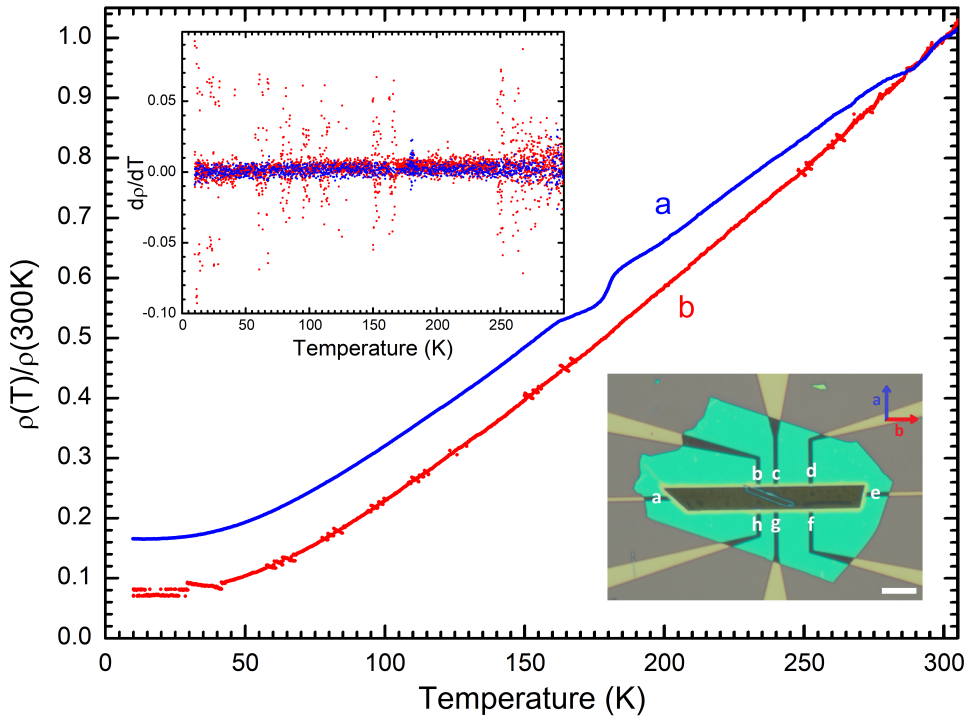

Figure 9: Acquired resistivity-temperature characteristic for longitudinal and transverse temperature sweeps. Longitudinal first harmonic voltage was measured over contacts *c* and *d* (thus excluding the contact resistance). Transverse first harmonic voltage was measured over contacts *d* and *f* (thus including the contact resistance). The bottom right inset shows an overview of the contacts with crystal directions indicated. The top left inset shows the derivative of the resistivity as a function of temperature.

Note that there is a resistance anisotropy for the two crystal directions shown. The relative resistivity in the *a*-direction is higher than in the *b*-direction up until $T = 285$K. After 285K, the graphs follow a similar path. Towards $T = 0$K, both graphs differ. By extrapolating the graphs to extract a value for ρ(0K), the *RRR* can be calculated. In the *a*-direction, ρ(0K) = 0.17 ± 0.01 ρ(300K) which gives $RRR_a = 5.9 \pm 0.4$. In the *b*-direction, ρ(0K) = 0.08 ± 0.01 ρ(300K), yielding $RRR_b = 12.5 \pm 1.6$.

To check for any slight changes in slope of either graph, the upper left inset is included in Fig. 9. This inset shows the derivative of the resistivity with respect to temperature for both the a- and b-direction, with color indication identical to the colors in the main graph. Note that peaks in this inset indicate a sudden change in slope, which may signify the 'bump' in the ρ(T)/ρ(300K) to T graph caused by the CDW. In the a-direction, a 'bump' is seen around $T = 180$K (with accompanying peak in the dρ/dT graph). This can, however, not be attributed to a CDW. The 'bump' in this part of the graph was caused by a change in the He flow through the setup, after which the heater had to adjust to the new cooling rate. The suddenly decreased heating rate and the delay until the heating rate restabilized was not picked up by the thermometer, hence a 'bump' is seen in the graph. In the b-direction, a series of 'small bumps' are also seen between $T = 0$K and $T = 40$K, and within 5K ranges around $T = 65$K, $T = 82$K, $T = 98$K, $T = 115$K, $T = 129$K, $T = 160$K and $T = 176$K. These 'bumps' also have corresponding peaks in the dρ/dT graph, where it can be clearly seen that these peaks periodically appear with a period of about 16K (with an exception of an expected peak around $T = 145$K). Between $T = 176$K and $T = 250$K the peaks disappear, but from $T = 255$K the 16K periodic pattern continues. The regular behavior of the peaks suggests they are a result of systematic error in the system, such as a periodic He flow leak, a heater calibration error or a systematic measurement error in the apparatus. As a result of the considerations of the origins of the peaks in both the a-direction and the b-direction, it can be decisively concluded that no CDW signature is seen in Fig. 9.

4.5 Second Harmonic Signal

The following data were found for the second harmonic Hall voltage, measured perpendicular to the direction in which the current was applied. The red graphs Fig. 10**a,b** are two repetitions of the same measurement, with a current applied from contact a to e and a second harmonic measured over contacts d and f. The blue graph in Fig. 10**b**, the current was applied from f to d and the second harmonic measured over c and d.

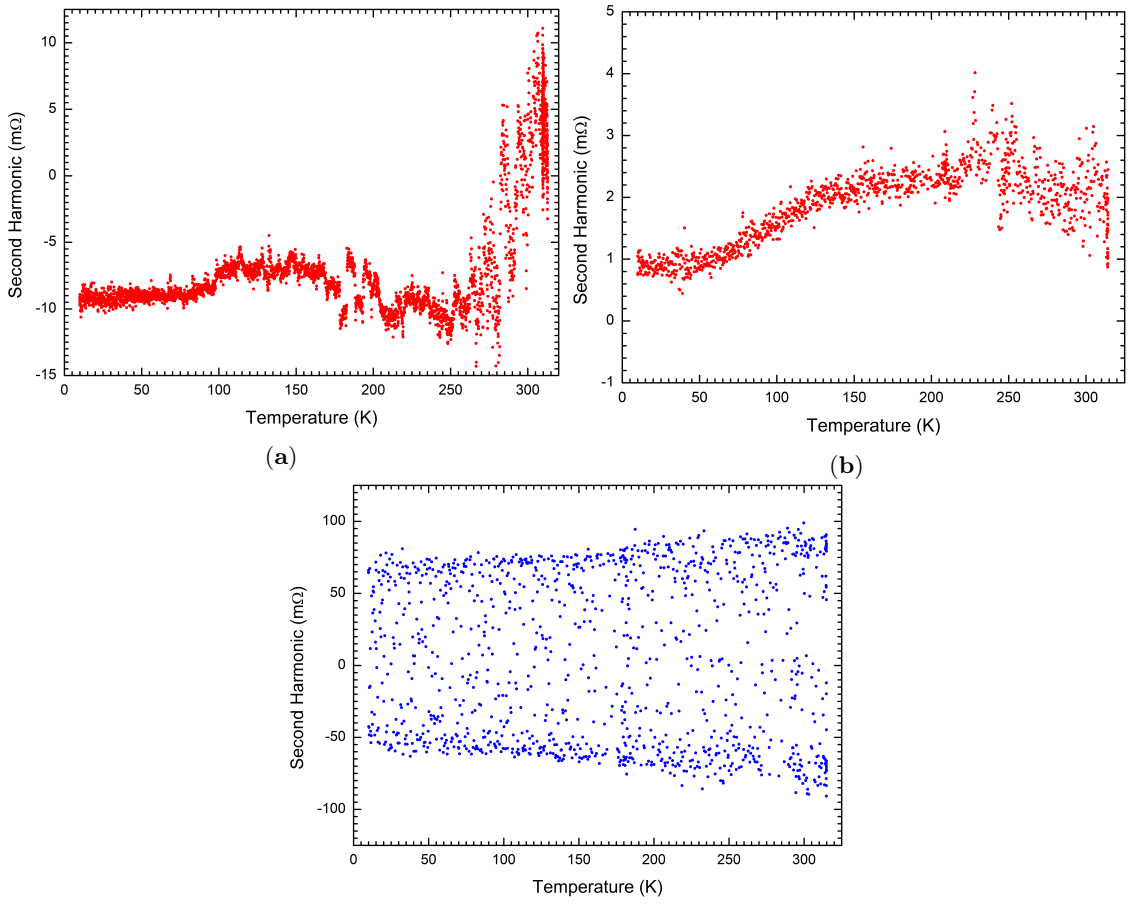

Figure 10: Graphs of the second order harmonic voltage signal measured along a (**a** & **b**) and along b (**c**).

5 Discussion and Outlook

The resistivity found in the b direction of $\rho_b = 98 \pm 12$ μΩ·cm is in good accordance with literature. It is within the ranges mentioned in *Theoretical Framework*. Felser and colleagues report a resistivity of about 75 μΩ·cm in the a and about 140 μΩ·cm b direction at room temperature [20], while Zhu et al. reports a resistivity that is aproximately equal in the a and b direction, of about 120 ± 20 μΩ·cm [21].

However, the resistivity is the only measured quantity that is in good accordance with literature. The second order Hall signals in Fig. 10**a,b** are too different to come to an agreeable average, and also seem to be random. Thus, a clear, noise-free second harmonic hall voltage was not observed. Also, the second harmonic Hall voltage signal observed did not vanish beyond the range where it was expected to occur: from 0K to 300K the second harmonic persisted, possibly indicating a constant noise in the apparatus instead of a true signal due to the CDW.

Indeed, the absence of a CDW can be confirmed, as stated in section 4.4. Even when extracting the derivative of resistivity to check for a slight 'bump' in the curve, there was no statistically significant signature of the CDW. The resistivity graphs are smooth (with exception of some noise) and do not show the 'bump' expected from literature. There are multiple possible reasons for this null result. In section 2.4.1, it is briefly mentioned that CDW formation in $ZrTe_3$ is very sensitive to crystallographic defects: impurities and intercalation by various atom types. The supplier of our $ZrTe_3$ crystals pointed out that the crystals were slightly oxidized. (Here, *oxidized* means *has chemically reacted with oxygen*, and does not refer to the various oxidation states in which Te is present in pure $ZrTe_3$.) The fact that the flake was oxidized might have already quenched the CDW to such an extent that it was not visible. For further research it is essential that the sample used is pure.

There is a more interesting reason why the CDW might not have been visible. In 2019, Hooda et al. made a distinction between 'flake' and 'needle' structures of $ZrTe_3$ [31]. The 'needle' structure does not exhibit a 'bump' in the resistivity graph, thus showing there is no CDW formation in this structure. If the flake we used can be classified as a 'needle'-like structure according to Hooda et al., this might explain the negative result. However, Hooda and colleagues do not go in depth on these classifications and only mention them twice throughout the article. For further research I would suggest manufacturing multiple samples, each with $ZrTe_3$ flakes of differing dimensions and different flake thicknesses to see whether the CDW appears. However, to detect a second order Hall voltage, the flake will also probably have to be only a few layers thick. The boundaries on which a material can be treated as bulk or can be called few-layer, has yet to be determined for $ZrTe_3$.

Another reason why the CDW was not visible might be the high contact resistance. Each contact was estimated to have a resistance of 0.97 ± 0.1 kΩ. This is about two orders of magnitude higher than the resistance of the flake itself, which makes the CDW signal more difficult to visualize and makes the measurements more sensitive to noise. If the contacts' edges weren't so rounded, the contact area between the flake and the contacts would be larger, possibly reducing the contact resistance. For further research I would recommend using wider contacts (not 1μm, but more than ~5um) to increase the touching area between the contacts and the flake, thus significantly decreasing contact resistance.

6 Conclusions

In conclusion, no CDW was detected in $ZrTe_3$. This prevented the second order Hall detection as well, as the required symmetry breaking via the CDW did not occur. However, a characterization of $ZrTe_3$ could be done, which has yielded a resistivity-temperature graph with a clear anisotropic resistivity in the material, as expected from literature.

There are a few possible reasons why the CDW was not detected. The apparent high sensitivity to impurities literature describes for CDW formation in $ZrTe_3$, is expected to be the largest factor, as the sample was slightly oxidized. The RRRs found can confirm this, as they were quite low: $RRR_a = 5.9 \pm 0.4$ and $RRR_b = 12.5 \pm 1.6$ in the crystal a- and b-directions respectively. In comparison, in copper a RRR of 10 000 could be reached [32]. Also, the high contact resistance (in the order of kΩs) compared to the flake resistance (in the order of few Ωs) might have quenched the CDW signal. A more exotic explanation might be different internal electron transport effects for 'needles' or 'flakes' as mentioned by Hooda and colleagues [31], but this is speculative and requires more research.

Acknowledgements

I would like to thank Anna for the daily supervision and the help in the lab. I thank Marcos for his enthusiasm and the engaging lectures on Berry curvature.

References

[1] A. K. Geim and K. S. Novoselov, "The rise of graphene," *Nature Materials*, vol. 6, pp. 183–191, 3 2007. DOI: 10.1038/nmat1849.

[2] P. Vogt, P. De Padova, C. Quaresima, J. Avila, E. Frantzeskakis, M. C. Asensio, A. Resta, B. Ealet and G. Le Lay, "Silicene: Compelling Experimental Evidence for Graphenelike Two-Dimensional Silicon," *Physics Review Letters*, vol. 108, p. 155 501, 15 2012. DOI: 10.1103/PhysRevLett.108.155501.

[3] M. E. Dávila, L. Xian, S. Cahangirov, A. Rubio and G. L. Lay, "Germanene: A novel two-dimensional germanium allotrope akin to graphene and silicene," *New Journal of Physics*, vol. 16, no. 9, p. 095 002, 2014. DOI: 10.1088/1367-2630/16/9/095002.

[4] F. F. Zhu, W. J. Chen, Y. Xu, C. L. Gao, D. D. Guan, C. H. Liu, D. Qian, S. C. Zhang and J. F. Jia, "Epitaxial growth of two-dimensional stanene," *Nature Materials*, 2015. DOI: 10.1038/nmat4384.

[5] H. Liu, A. T. Neal, Z. Zhu, Z. Luo, X. Xu, D. Tománek and P. D. Ye, "Phosphorene: An Unexplored 2D Semiconductor with a High Hole Mobility," *ACS Nano*, vol. 8, no. 4, pp. 4033–4041, 2014, PMID: 24655084. DOI: 10.1021/nn501226z.

[6] S. Z. Butler, S. M. Hollen, L. Cao, Y. Cui, J. A. Gupta, H. R. Gutiérrez, T. F. Heinz, S. S. Hong, J. Huang, A. F. Ismach, E. Johnston-Halperin, M. Kuno, V. V. Plashnitsa, R. D. Robinson, R. S. Ruoff, S. Salahuddin, J. Shan, L. Shi, M. G. Spencer, M. Terrones, W. Windl and J. E. Goldberger, "Progress, Challenges, and Opportunities in Two-Dimensional Materials Beyond Graphene," *ACS Nano*, vol. 7, no. 4, pp. 2898–2926, 2013, PMID: 23464873. DOI: 10.1021/nn400280c.

[7] J. Dai, M. Li and X. C. Zeng, "Group IVB transition metal trichalcogenides: A new class of 2D layered materials beyond graphene," *WIREs Computational Molecular Science*, vol. 6, no. 2, pp. 211–222, 2016. DOI: https://doi.org/10.1002/wcms.1243.

[8] M. V. Berry, "Quantal phase factors accompanying adiabatic changes," *Proceedings of the Royal Society A*, vol. 392, pp. 45–57, 1984. DOI: 10.1098/rspa.1984.0023.

[9] I. Sodemann and L. Fu, "Quantum nonlinear Hall effect induced by Berry curvature dipole in time-reversal invariant materials," *Physical Review Letters*, vol. 115, no. 21, 2015, ISSN: 1079-7114. DOI: 10.1103/physrevlett.115.216806.

[10] J. C. Maxwell, *A Treatise on Electricity and Magnetism*. Clarendon Press, 1873, vol. 2, p. 144.

[11] E. H. Hall, "On a new action of the magnet on electric currents," *American Journal of Mathematics*, vol. 2, pp. 287–292, 1879. [Online]. Available: https://www.jstor.org/stable/2369245.

[12] L. D. Landau, E. M. Lifshitz and L. P. Pitaevskii, *Statistical Physics*, 3rd ed., ser. Course of Theoretical Physics. Oxford: Pergamon Press, 1999, vol. 5.

[13] K. Kang, T. Li, E. Sohn, J. Shan and K. F. Mak, "Nonlinear anomalous Hall effect in few-layer WTe_3," *Nature Materials*, vol. 18, pp. 324–328, 4 2019, ISSN: 1476-4660. DOI: 10.1038/s41563-019-0294-7.

[14] J. Bardeen, L. N. Cooper and J. R. Schrieffer, "Theory of superconductivity," *Physics Review*, vol. 108, pp. 1175–1204, 5 1957. DOI: 10.1103/PhysRev.108.1175.

[15] E. You, *Difference between charge density wave (CDW) and superconductivity?* Physics Stack Exchange, (version: 2017/06/19). [Online]. Available: https://physics.stackexchange.com/q/339411 (visited on 23/06/2021).

[16] C. Wayman and H. Bhadeshia, "Chapter 16 - phase transformations, nondiffusive," in *Physical Metallurgy (Fourth Edition)*, R. W. Cahn and P. Haasen†, Eds., Fourth Edition, Oxford: North-Holland, 1996, pp. 1507–1554, ISBN: 978-0-444-89875-3. DOI: https://doi.org/10.1016/B978-044489875-3/50021-1.

[17] R. Peierls, *Quantum Theory of Solids*. New York: Oxford University, 1955.

[18] T. Yokoya, T. Kiss, A. Chainani, S. Shin and K. Yamaya, "Role of charge-density-wave fluctuations on the spectral function in a metallic charge-density-wave system," *Phys. Rev. B*, vol. 71, p. 140 504, 14 2005. DOI: 10.1103/PhysRevB.71.140504.

[19] J. Laverock, S. B. Dugdale, Z. Major, M. A. Alam, N. Ru, I. R. Fisher, G. Santi and E. Bruno, "Fermi surface nesting and charge-density wave formation in rare-earth tritellurides," *Phys. Rev. B*, vol. 71, p. 085 114, 8 2005. DOI: 10.1103/PhysRevB.71.085114.

[20] C. Felser, E. W. Finckh, H. Kleinke, F. Rocker and W. Tremel, "Electronic properties of $ZrTe_3$," *Journal of Material Chemistry*, vol. 8, pp. 1787–1798, 8 1998. DOI: 10.1039/A802948B.

[21] X. Zhu, W. Ning, L. Li, L. Ling, R. Zhang, J. Zhang, K. Wang, Y. Liu, L. Pi, Y. Ma, H. Du, M. Tian, Y. Sun, C. Petrovic and Y. Zhang, "Superconductivity and charge density wave in $ZrTe_{3x}Se_x$," *Scientific Reports*, vol. 6, 1 2016.

[22] C. S. Yadav and P. L. Paulose, "Superconductivity at 5.2 K in $ZrTe_3$ polycrystals and the effect of Cu and Ag intercalation," *Journal of Physics: Condensed Matter*, vol. 24, p. 235 702, 2012. DOI: 10.1088/0953-8984/24/23/235702.

[23] X. Zhu, B. Lv, F. Wei, Y. Xue, B. Lorenz, L. Deng, Y. Sun and C.-W. Chu, "Disorder-induced bulk superconductivity in $ZrTe_3$ single crystals via growth control," *Physics Review B*, vol. 87, p. 024 508, 2 2013. DOI: 10.1103/PhysRevB.87.024508.

[24] R. Yomo, K. Yamaya, M. Abliz, M. Hedo and Y. Uwatoko, "Pressure effect on competition between charge density wave and superconductivity in $ZrTe_3$: Appearance of pressure-induced reentrant superconductivity," *Phys. Rev. B*, vol. 71, p. 132 508, 13 2005. DOI: 10.1103/PhysRevB.71.132508.

[25] M. Hoesch, L. Gannon, K. Shimada, B. J. Parrett, M. D. Watson, T. K. Kim, X. Zhu and C. Petrovic, "Disorder Quenching of the Charge Density Wave in $ZrTe_3$," *Physical Review Letters*, vol. 122, no. 1, 2019, ISSN: 1079-7114. DOI: 10.1103/physrevlett.122.017601.

[26] Y. Hu, F. Zheng, X. Ren, J. Feng and Y. Li, "Charge density waves and phonon-electron coupling in $ZrTe_3$," *Phys. Rev. B*, vol. 91, p. 144 502, 14 2015. DOI: 10.1103/PhysRevB.91.144502.

[27] J. P. Hirth and J. Lothe, *Theory of dislocations*, 2nd ed. Krieger Publishing Company, 1992, ISBN: 978-0-89464-617-1.

[28] T. Banerjee, personal communication, 2020.

[29] P. J. Zomer, M. H. D. Guimarães, J. C. Brant, N. Tombros and B. J. van Wees, "Fast pick up technique for high quality heterostructures of bilayer graphene and hexagonal boron nitride," *Applied Physics Letters*, vol. 105, p. 013 101, 2014. DOI: 10.1063/1.4886096.

[30] M. H. D. Guimarães, *Spin and charge transport in graphene devices in the classical and quantum regimes*, PhD Thesis, Groningen, 2015.

[31] M. Hooda, T. Tripathi and C. Yadav, "Semiconducting nature and thermal transport studies of $ZrTe_3$," *Journal of Alloys and Compounds*, vol. 785, pp. 603–609, 2019, ISSN: 0925-8388. DOI: https://doi.org/10.1016/j.jallcom.2019.01.136.

[32] S. Rosenblum, W. Steyert and F. Fickett, "A simple method for producing high conductivity copper for low temperature applications," *Cryogenics*, vol. 17, no. 11, pp. 645–647, 1977, ISSN: 0011-2275. DOI: https://doi.org/10.1016/0011-2275(77)90123-0.

Appendix A Derivations

The derivations of the equations in *Theoretical Framework* are given here. Eq. (3) can be derived from Eq. (2) in the following manner:

$$\begin{aligned}
\mathbf{E} &= \frac{\mathbf{p}}{q\tau} - \mathbf{v}\times\mathbf{B} \\
&= \frac{m}{nq^2\tau}\mathbf{j} - \frac{1}{nq}\mathbf{j}\times\mathbf{B} \\
&= \left(\frac{m}{nq^2\tau} + \frac{1}{nq}\mathbf{B}\times\right)\mathbf{j} \\
&= \frac{1}{nq}\left(\frac{m}{q\tau} + \mathbf{B}\times\right)\mathbf{j} \\
&= \frac{1}{nq}\left(\frac{m}{q\tau} + \begin{bmatrix} B_x \\ B_y \\ B_z \end{bmatrix}\times\right)\begin{bmatrix} j_x \\ j_y \\ j_z \end{bmatrix} \\
&= \frac{1}{nq}\left(\begin{bmatrix} \frac{m}{q\tau} & 0 & 0 \\ 0 & \frac{m}{q\tau} & 0 \\ 0 & 0 & \frac{m}{q\tau} \end{bmatrix} + \begin{bmatrix} 0 & -B_z & B_y \\ B_z & 0 & -B_x \\ -B_y & B_x & 0 \end{bmatrix}\right)\begin{bmatrix} j_x \\ j_y \\ j_z \end{bmatrix} \\
&= \frac{1}{nq}\begin{bmatrix} \frac{m}{q\tau} & -B_z & B_y \\ B_z & \frac{m}{q\tau} & -B_x \\ -B_y & B_x & \frac{m}{q\tau} \end{bmatrix}\begin{bmatrix} j_x \\ j_y \\ j_z \end{bmatrix}.
\end{aligned}$$

Here, $\mathbf{E}$ and $\mathbf{B}$ are the current generating electric field and the external magnetic field respectively. A number of n current carrying particles with charge q, velocity $\mathbf{v}$ and mass m, lose their momentum $\mathbf{p} = m\mathbf{v}$ to lattice vibrations during a relaxation time τ. The particles together generate a current density $\mathbf{j} = nq\mathbf{v}$.

Eq. (7) can be derived from Eq. (6) by substitution of an alternating (AC) current $I(t) = I_0 \sin(\omega t + \phi_0)$ (with amplitude I_0, frequency ω and phase ϕ_0):

$$\begin{aligned}
V_H(t) &= R_0 I_0 \sin(\omega t + \phi_0) + R_1 (I_0 \sin(\omega t + \phi_0))^2 \\
&= R_0 I_0 \sin(\omega t + \phi_0) + R_1 I_0^2 \sin^2(\omega t + \phi_0) \\
&= R_0 I_0 \sin(\omega t + \phi_0) + R_1 I_0^2 \left(\frac{1}{2} - \frac{1}{2}\cos(2\omega t + 2\phi)\right) \\
&= R_0 I_0 \sin(\omega t + \phi_0) + \frac{1}{2} R_1 I_0^2 + \frac{1}{2} R_1 I_0^2 \sin(2\omega t + 2\phi - \frac{\pi}{2}) \\
&= R_0 I_0 \sin(\omega t + \phi_0) + \frac{1}{2} R_1 I_0^2 + \frac{1}{2} R_1 I_0^2 \sin(2\omega t + \phi_1) \qquad \text{with} \quad \phi_1 = 2\phi_0 - \frac{\pi}{2}
\end{aligned}$$

where $V_H(t)$ is the time-dependent Hall voltage and R_0 and R_1 are the zeroth and first order Hall resistances.

Appendix B Flake resistance estimation

To estimate the contact resistance, the longitudinal flake resistance R_F must be estimated first. The flake resistance can then be subtracted from the entire resistance along the (two-probe) path from contact a to e. The resistance values from Table 1 are used to estimate the flake resistance R_{FT} of the 15 µm long part of the $ZrTe_3$ flake between contacts b (h) and d (f). The cursive typeset numbers are not taken into account in the estimation, as they are treated as outliers. Averaging of values in the table below gives $R_{F1} = 4.5 \pm 0.2\ \Omega$, $R_{F2} = 12.7 \pm 0.9\ \Omega$, $R_{FT} = 17.0 \pm 0.7\ \Omega$. Errors are chosen such that 68% of observations (one standarddeviation above and below calculated value) fall within the bounds. From R_{F1} and R_{F2}, also a calculated value of R_{FT} can be arrived at: $R_{FT,calc} = R_{F1} + R_{F2} = 17.2 \pm 1\ \Omega$. Together with the initially measured R_{FT}, this can be averaged to a final R_{FT} of $17.1 \pm 0.6\ \Omega$.

I_+	I_-	V_+	V_-	I_{in} (mA)	gain	V_{out} (mV)	R (Ω)	Phase (°)
a	e	b	d	1.0	1000x	18.5	18.5	-1.68
a	e	b	c	1.0	1000x	4.5	4.5	-20
a	e	c	d	1.0	1000x	14.01	14.01	4.81
a	e	h	f	1.0	100x	*29.5*	*295*	1.30
a	e	h	g	1.0	100x	*27.9*	*279*	1.44
a	e	g	f	1.0	100x	1.26	12.6	-1.80
b	d	h	f	1.0	1000x	16.46	16.46	-0.95
b	d	h	g	1.0	1000x	4.60	4.60	-2.60
b	d	g	f	1.0	1000x	11.87	11.87	-0.05
h	f	b	d	1.0	1000x	16.50	16.50	-0.45
h	f	b	c	1.0	1000x	4.39	4.39	-10.91
h	f	c	d	1.0	1000x	12.18	12.18	4.01
h	d	b	f	1.0	1000x	16.69	16.69	0.58
b	f	h	d	1.0	1000x	16.33	16.33	-1.80
b	e	h	f	1.0	1000x	16.98	16.98	-3.32
h	e	b	d	1.0	1000x	17.57	17.57	-1.90

Table 1: Four-probe measurements done at $T = 295$K, with an AC current with input frequency $\omega = 17.77$ Hz. The first four columns indicate the wire connections to the various contacts. The fifth and seventh column indicate the input current I_{in} and output voltage respectively. The resistance R in the eight column is calculated from I_{in}, V_{out} and the gain (sixth column). The last column indicates the phase difference between I_{in} and V_{out}.

The distance between contacts a and e is measured to be 26 µm (see Fig. 4 in the *Sample fabrication* section (3.1)). Assuming the current flows only through the part of the flake between contacts a and e, so not over the length of the entire ~55 micron flake, R_F can be taken to be $R_F = R_{FT} \cdot \frac{26\mu m}{15\mu m} = 29.6 \pm 1\ \Omega$.